Article

Fabrication of Mn-Doped SrTiO₃/Carbon Fiber with Oxygen Vacancy for Enhanced Photocatalytic Hydrogen Evolution

Qi Hu [1,2], Jiantao Niu [3], Ke-Qin Zhang [1,*] and Mu Yao [4]

1   National Engineering Laboratory for Modern Silk, College of Textile and Clothing Engineering, Soochow University, Suzhou 215123, China; huqi@usts.edu.cn
2   School of Social Development and Public Administration, Suzhou University of Science and Technology, Suzhou 215009, China
3   School of Textile and Clothing and Arts and Media, Suzhou Institute of Trade and Commerce, Suzhou 215009, China; tjpunjt@126.com
4   School of Textile Science and Engineering, Xi'an Polytechnic University, Xi'an 710048, China; yaomu1930@163.com
*   Correspondence: kqzhang@suda.edu.cn; Tel.: +86-512-67061169

Abstract: With carbon fiber, it is difficult to load semiconductor photocatalysts and easy to shed off thanks to its smooth surface and few active groups, which has always been a problem in the synthesis of photocatalysts. In the study, SrTiO₃ nanoparticles were loaded onto the Tencel fibers using the solvothermal method, and then the Tencel fibers were carbonized at a high temperature under the condition of inert gas to form carbon fibers, thus SrTiO₃@CF photocatalytic composite materials with solid core shell structure were prepared. Meanwhile, Mn ions were added into the SrTiO₃ precursor reagent in the solvothermal experiment to prepare Mn-doped Mn-SrTiO₃@CF photocatalytic composite material. XPS and EPR tests showed that the prepared Mn-SrTiO₃@CF photocatalytic composite was rich in oxygen vacancies. The existence of these oxygen vacancies formed oxygen defect states (VOs) below the conduction band, which constituted the capture center of photogenerated electrons and significantly improved the photocatalytic activity. The photocatalytic hydrogen experimental results showed that the photocatalytic hydrogen production capacity of Mn-SrTiO₃@CF composite material with 5% Mn-doped was six times that of the SrTiO₃@CF material, and the doping of Mn ions not only promoted the red shift of the light absorption boundary and the extension to visible light, but also improved the separation and migration efficiency of photocarriers. In the paper, the preparation method solves the difficulty of loading photocatalysts on CF and provides a new design method for the recycling of catalysts, and we improve the hydrogen production performance of photocatalysts by Mn-doped modification and the introduction of oxygen vacancies, which provides a theoretical method for the practical application of hydrogen energy.

Keywords: SrTiO₃; hydrogen evolution; carbon fiber; oxygen vacancy

1. Introduction

As a sustainable green technology, semiconductor photocatalysis can transform solar energy, purify the environment, and produce renewable energy. At present, there are various kinds of semiconductor photocatalysts. Among them, SrTiO₃ semiconductor material has been widely used in fields such as photocatalytic water splitting hydrogen production, virus inactivation, and pollutant treatment thanks to its characteristics of excellent chemical stability, non-toxicity, low cost, good photoelectric property, and environmental friendliness [1]. However, powder SrTiO₃ photocatalytic material is easy to condense into blocks in use, which reduces the photocatalytic property of SrTiO₃, and causes some problems such as difficulties in the recycling of catalyst, easy consumption, possible secondary pollution, and so on, limiting its practical application. Therefore, some researchers have begun to think about loading photocatalysts on more suitable carriers [2]. Carbon fiber (CF) has

the advantages of a large specific surface area, high specific strength, high flexibility, and strong response to visible light, greatly improving the photocatalytic activity and stability of semiconductor photocatalysts; therefore, it is an ideal carrier for supporting granular semiconductor photocatalysts [3–5].

Similar to TiO_2 photocatalysts, pure $SrTiO_3$ has a large band gap (about 3.2 eV), resulting in its response to ultraviolet light accounting for a small amount of energy of sunlight, which severely limits the application of $SrTiO_3$ in the field of visible light photocatalysis. Therefore, to improve the photocatalytic property of $SrTiO_3$, modification strategies such as ion doping, co-catalyst loading, surface defect modification, and semiconductor heterojunction compounding have been proposed and further studied by researchers [1,6]. Ion doping is considered to be an effective method to improve the photocatalytic property of $SrTiO_3$. Common metal ions doped include Pt, Ag, Au, Ru, Pd, Cu, Al, Mn, and so on [7–14]. Mn-doped $SrTiO_3$ photocatalytic materials can reduce the band gap, while the preparation technology is mature and has been well developed and applied in the field of photocatalysis and widely used in the fields of photocatalytic degradation and photocatalytic water splitting hydrogen production [13,15,16]. Another effective method to improve the photocatalytic property of $SrTiO_3$ is surface defect modification [17]. Oxygen vacancy is a research hotspot in defect engineering. The introduction of oxygen vacancy can solve the problems of low light absorption efficiency of photocatalysts, rapid recombination of photoelectrons and holes, and lack of surface active sites, and is proved to be an important and effective strategy to improve photocatalytic efficiency [18–21]. Therefore, the introduction of oxygen vacancies in the preparation of $SrTiO_3$ photocatalytic material has attracted the attention of researchers.

How to combine the method of regulating the band gap by doping with the method of constructing surface defects by introducing oxygen vacancies is one kind of research approach to improve the photocatalytic property of $SrTiO_3$. In addition, carbon fibers (CFs) can be loaded into $SrTiO_3$ photocatalytic composite material as a photocatalyst carrier in consideration of difficulties in the recovery and recycling of photocatalysts. Previous studies on carbon fibers as a photocatalyst carrier have been reported, which basically found the following: carbon fibers were prepared first, and then the photocatalyst was loaded onto the carbon fibers. Such a method has problems including poor load stability and easy shedding of semiconductor materials [22–24]. How to prepare a highly stable $SrTiO_3$/carbon fiber by firmly loading the catalyst onto carbon fibers is a research focus of this paper.

In this paper, the two methods of Mn doping and introduction of oxygen vacancies were combined. With Tencel fibers as the carrier, an Mn-doped $SrTiO_3$ photocatalyst was loaded onto the surface of Tencel fibers by the solvothermal method, then the Tencel fibers were carbonized under the condition of argon, Mn-$SrTiO_3$@CF with a core shell structure rich in oxygen vacancies was successfully prepared, and the photocatalytic hydrogen production mechanism was discussed.

2. Experiment Section

2.1. Preparation of Photocatalytic Material

Preparation of Mn-$SrTiO_3$@Tencel Fiber Composite Fiber. The surface of Tencel fibers was coated with Mn-doped strontium titanate photocatalyst by the solvothermal method. Here, 15 mL of ethylene glycol and 19 mL of absolute ethyl alcohol were mixed and stirred well to form a mixed solvent. Then, 0.036 g of manganese acetate and 0.58 g of strontium acetate were added to the mixed solvent and stirred at room temperature for 30 min, and the above mixed solution was transferred to the PTFE reactor, wherein the molar ratio of manganese acetate to strontium acetate was 1:19. Then, 0.85 g of isopropyl titanate drop solution was added to the above mixed solution and it was stirred for one more hour [25]. After that, 0.8 g of Tencel fibers was selected, torn by hands, and then completely immersed into the solution in the PTFE reactors. The reactors were put into an oven for solvothermal reaction at 180 °C for 7 h. After the reaction finished and the temperature was

reduced to room temperature, the Tencel fibers were removed, cleaned with absolute ethyl alcohol, and then dried in the oven at 60 °C for 24 h, thus obtaining the Mn-SrTiO$_3$@Tencel fiber material.

Similarly, without manganese acetate reagent, SrTiO$_3$@Tencel fiber composite fibers were prepared according to the above experimental method, and the pure SrTiO$_3$ nanometer material was also prepared.

Preparation of Mn-SrTiO$_3$@CF Composite Fiber. Under the condition of inert gas, the tencel fibers were carbonized at a high temperature to prepare carbon fibers [26], which transformed Mn-SrTiO$_3$@Tencel fiber into Mn-SrTiO$_3$@CF material, and the specific experimental steps were as follows. First, the Mn-SrTiO$_3$@Tencel fiber was put into a crucible and then into a tube furnace, and the Tencel fibers were carbonized at 800 °C for 2 h under the condition of argon atmosphere while the heating rate was 5 °C/min, thus Mn-SrTiO$_3$@CF composite material with a core shell structure was obtained.

Under the same process conditions, SrTiO$_3$@CF was prepared.

2.2. Characterization Method

The crystalline structures of the samples were characterized by an X-ray diffractometer (XRD, Bruker D8 Disvover, Bruker, Karlsruhe, Germany) at a scanning speed of 0.2 °/min, and the morphologies of the as-prepared products were characterized by an electron microscope (FESEM Hitachi S-4800) and a transmission electron microscope (TEM FEI talos F200x G2). The binding energy was detected by X-ray photoelectron spectroscopy (XPS, Thermo Scientific K-Alpha, Thermo Fisher Scientific, Horsham, UK), and the defects of the samples were tested and characterized by an electronic paramagnetic spectrometer (EPR, Bruker EMX PLUS, Bruker, Karlsruhe, Germany) with a sweep width of 50 G. The electrochemical impedance and Mott–Schottky curve of the samples were tested by an electrochemical workstation (CHI660E) with the standard three-electrode testing method. The UV–Vis diffuse reflectance spectra (DRS) were obtained by a Hitachi F-7000 spectro-photometer.

2.3. Photocatalytic Evolution

The photocatalytic hydrogen evolution of the samples was tested through a gas chromatograph (GC-7900, Techcomp (China) Co., Ltd., Shanghai, China), which was used to measure the hydrogen production of samples under simulated sunlight irradiation. Before the experiment, 100 mg of catalyst sample was added into the mixture of 50 mL of Na$_2$S (0.35 M) solution and 50 mL of Na$_2$SO$_3$ (0.25 M) solution, wherein Na$_2$S and Na$_2$SO$_3$ were used as sacrificial agents in the photocatalytic hydrogen production experiment. During the experiment, a PLS-SE300C 300 W xenon lamp was used to simulate the solar light source for testing.

3. Results and Discussion

The qualitative phase analysis and crystal structure analysis of photocatalysts could be carried out through an x-ray diffraction test. Figure 1 shows the XRD patterns of Mn-SrTiO$_3$@CF, SrTiO$_3$@CF, carbon fibers, and pure SrTiO$_3$. It can be observed from Figure 1 that the SrTiO$_3$@CF photocatalytic composite fibers have obvious diffraction peaks at 32.25°, 39.72°, 46.38°, 57.70°, 67.61°, and 76.85°, respectively, corresponding to (110), (111), (200), (211), (220), and (310) crystal faces of SrTiO$_3$ (PDF#35-0734), respectively, which indicates that the loaded SrTiO$_3$ has a cubic phase perovskite structure [27,28]. Mn-SrTiO$_3$@CF have basically the same diffraction peak positions and peak intensities as SrTiO$_3$@CF and have no new diffraction peak, from which it can be presumed that the doping of 5% Mn does not significantly change the crystal structure of the composite catalyst [13]. The above test analysis indicated that strontium titanate semiconductor material was successfully loaded on the surface of carbon fibers, but whether Mn was doped into the strontium titanate material needed to be further tested and verified.
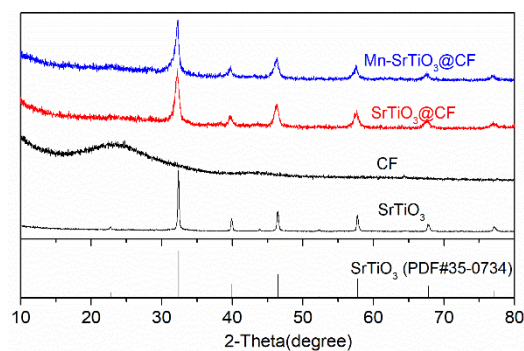
Figure 1. XRD pattern of samples.

The morphology characteristics of Mn-SrTiO$_3$@CF photocatalytic composite fibers and its preparation process can be further understood through an SEM test and characterization. As shown in Figure 2a,b, Tencel fibers are smooth-faced circular elongated fibers with a diameter of about 10 μm. Figure 2c shows the morphology structure of SrTiO$_3$@Tencel fiber prepared by the solvothermal method; paste-like SrTiO$_3$ particles are coated on the surface of Tencel fibers, and the diameter of SrTiO$_3$@Tencel fiber composite fibers is about 11 μm. It can also be seen from Figure 2c that the SrTiO$_3$ layer on the surface of Tencel fibers has obvious cracks, which may be caused by high pressure irradiation in the process of taking SEM pictures. This is because, under high pressure irradiation, the SrTiO3 material layer would split with the Tencel fiber. In this solvothermal experiment, the Tencel fibers did not dissolve in the high temperature solution because of the use of ethylene glycol and absolute ethyl alcohol as solvents, which effectively prevented cellulose fibers from dissolving. Figure 2d–f shows the morphology structure of SrTiO$_3$@CF composite fibers prepared after the Tencel fibers are carbonized at a high temperature to form carbon fibers, from which it can be observed that SrTiO$_3$ particles are closely coated on the surface of carbon fibers to form a coating layer with a core shell structure. SrTiO$_3$ particles are organically combined with carbon fibers by the high temperature carbonization process to form a firm and close whole. Interestingly, it can be observed from Figure 2f that SrTiO$_3$ nanoparticles have a cubic phase structure, which is consistent with the XRD test results of SrTiO$_3$@CF. In addition, it can be found by comparing Figure 2c,d that the diameter of carbon fibers formed by carbonizing Tencel fibers at a high temperature is reduced, and the diameter of the prepared SrTiO$_3$@CF composite fibers is 6–7 μm. Figure 2g–h is an SEM diagram of Mn-SrTiO$_3$@CF composite fibers prepared after doping of 5% Mn, with the surface morphology structure similar to that of SrTiO$_3$@CF composite fibers. Figure 2i shows an SEM diagram of the cross-section structure of Mn-SrTiO$_3$@CF composite fibers, from which it can be observed that the carbon fiber in the core of the composite material has a circular structure, and the thickness of the Mn-SrTiO$_3$ catalyst layer of the shell layer is about 100 nm.

To explore the distribution of various elements in the Mn-SrTiO$_3$@CF sample, the SEM mapping test was performed, and the results are shown in Figure 3. It can be observed from Figure 3b that the color of carbon fibers is lighter, which is consistent with the test results in [29]. This is because the SEM mapping test is mainly for the element distribution on the surface of the samples within a certain area, the Mn-SrTiO$_3$@CF composite fibers have a core shell structure, and the carbon fibers are in the coated state, so the content of C element detected in the Mn-SrTiO$_3$@CF is relatively small. As shown in Figure 3, elements such as Sr, Ti, Mn, and O are evenly distributed on the surface of carbon fibers, and the content of Mn is lower, which corresponds to the actual ratio.
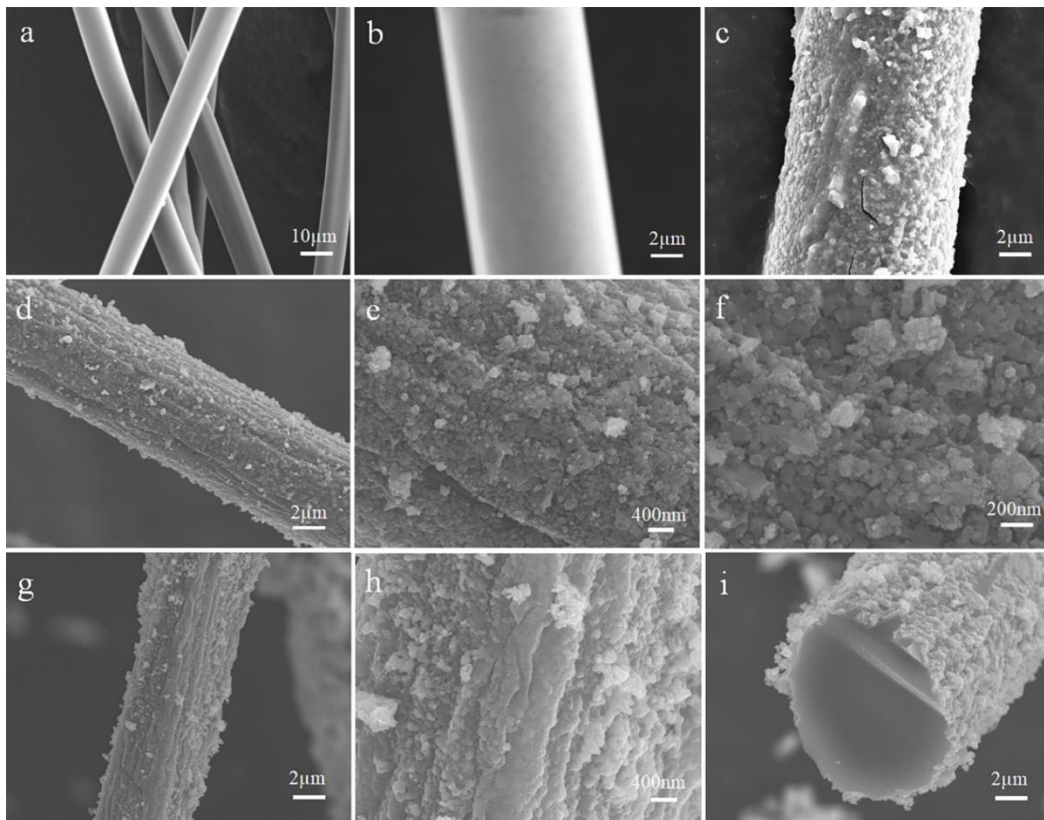
Figure 2. SEM diagram of samples: (**a**–**c**) Tencel fiber, (**c**) SrTiO$_3$@Tencel fiber, (**d**–**f**) SrTiO$_3$@CF, (**g**–**i**) Mn-SrTiO$_3$@CF.

Element	Wt%	Atomic percent
C	73.91	85.61
O	13.77	11.98
Ti	3.30	0.96
Mn	0.23	0.06
Sr	8.79	1.39
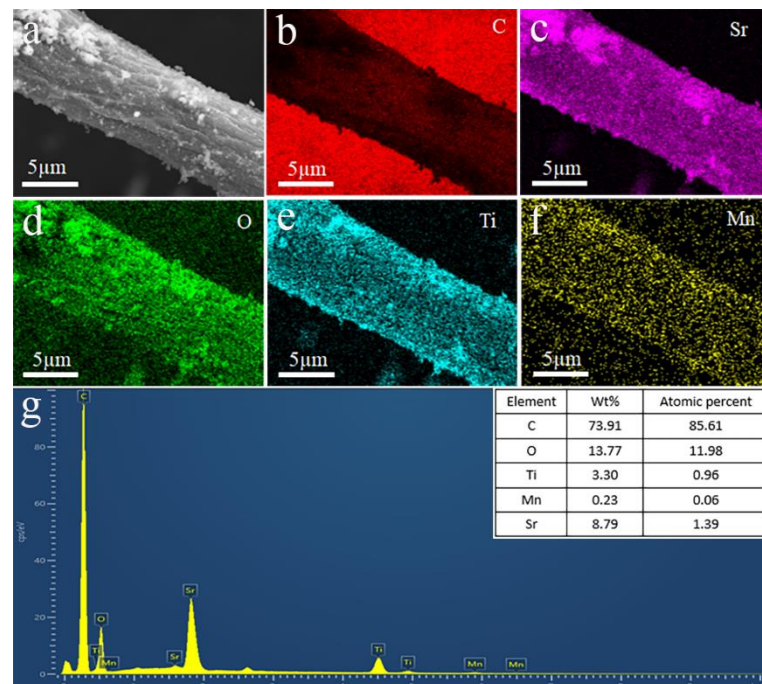
Figure 3. SEM mapping diagram of Mn-SrTiO$_3$@CF sample: (**a**) SEM diagram of composite fiber, (**b**) C element, (**c**) Sr element, (**d**) O element, (**e**) Ti element, (**f**) Mn element, and (**g**) element content diagram.

TEM and HRTEM of the Mn-SrTiO$_3$@CF sample are shown in Figure 4. SrTiO$_3$ plies observed in Figure 4a are nano-fragments shed from the Mn-SrTiO$_3$@CF sample that was cut into pieces, from which it can be seen that most of the SrTiO$_3$ plies are composed of small particles of 10–20 nm combined together, and these small nanoparticles have a larger specific surface area, which is conducive to improving the photocatalytic activity. The corresponding interplanar spacing shown in Figure 4c is about 0.279 nm, which shall belong to the (110) crystal face of SrTiO$_3$ (PDF#35-0734) [30]. The doping of a small amount of Mn may change the spacing of the crystal face, which is not significant. The above experimental results showed that Mn was successfully doped in the SrTiO$_3$ material [31], and the doping of a small amount of Mn does not significantly change the lattice structure of the SrTiO$_3$ material.
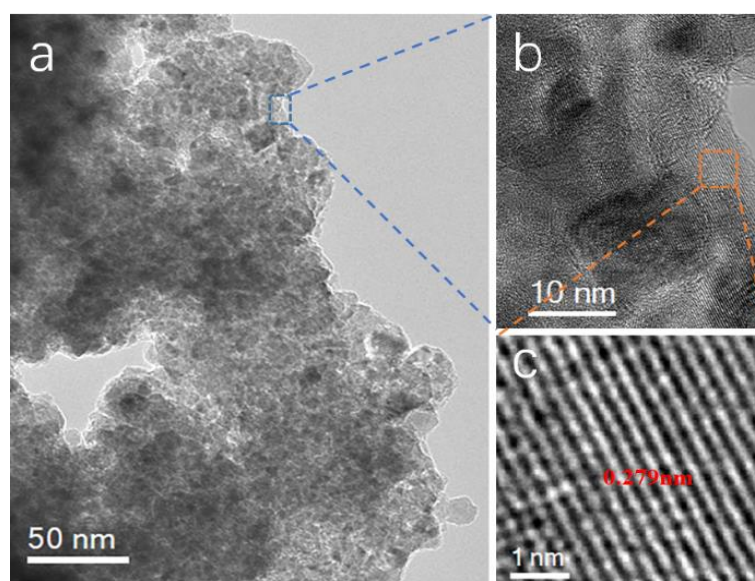

Figure 4. TEM diagram of the Mn-SrTiO$_3$@CF sample, (**a**) Mn-SrTiO$_3$ nanosheets, (**b**) HRTEM at the interface, and (**c**) HRTEM of Mn-SrTiO$_3$.

The composition and valence state of Mn-SrTiO$_3$@CF photocatalysts are researched through X-ray photoelectron spectroscopy (XPS). Figure 5 shows the full spectrum of the Mn-SrTiO$_3$@CF sample and the high-resolution XPS spectra of C 1s, Sr 3d, Ti 2p, O 1s, and Mn 2p. Figure 5a shows the full spectrum of the Mn-SrTiO$_3$@CF sample, indicating that there are mainly Sr, Ti, Mn, O, and C in the prepared sample, without other impurities. In the fitting spectrum of C 1s shown in Figure 5b, the fitting peak at 284.0 eV is a C–C bond, which corresponds to the C–C bond in carbon fibers and is partially similar to the graphite structure, while the fitting peak at 285.2 eV shall belong to a small amount of C–O bonds on the surface of carbon fibers [31]. It is presumed that carbon fibers and SrTiO$_3$ material are bonded partially through a chemical bond formed by O atoms. It can be observed from Figure 5c that the high resolution XPS spectrum of Ti 2p can be fitted into two characteristic peaks, which are located at the binding energies of 458.0 eV and 463.8 eV, respectively, which, presumably, shall belong to Ti 2p$_{3/2}$ and Ti 2p$_{1/2}$, respectively, corresponding to Ti^{4+} ions. The difference between the two fitting peaks is 5.8 eV [8]. It can be observed from the spectrum of Sr 3d shown in Figure 5d that peaks at the binding energies of 132.5 eV and 134.3 eV are attributed to Sr 3d$_{5/2}$ and Sr 3d$_{3/2}$ of Sr^{2+}, and the difference between the peaks is 1.8 eV [32]. Interestingly, as shown in Figure 5e, the peak of O 1s is fitted into three peaks that are located at 529.2 eV, 530.9 eV, and 532.4 eV, respectively, wherein the peak at the binding energy of 529.2 eV corresponds to lattice oxygen in SrTiO$_3$, while the peak at the binding energy of 530.9 eV may be adsorption oxygen in oxygen vacancy, and the peak at 532.4 eV corresponds to surface adsorption oxygen in the SrTiO$_3$ catalyst. This test indicated that there may be oxygen vacancies in the Mn-SrTiO$_3$@CF

catalyst sample [33,34], which needs to be further confirmed by the EPR test. Figure 5f shows the high-resolution XPS diagram of Mn 2p. Because of the low content of doped Mn, the corresponding measured XPS characteristic peak signal is relatively weak. After peak fitting, it is presumed that the characteristic peaks located at the binding energies of 641.6 eV and 652.6 eV correspond to Mn $2p_{3/2}$ and Mn $2p_{1/2}$, respectively, and the difference between the two peaks is 11 eV.
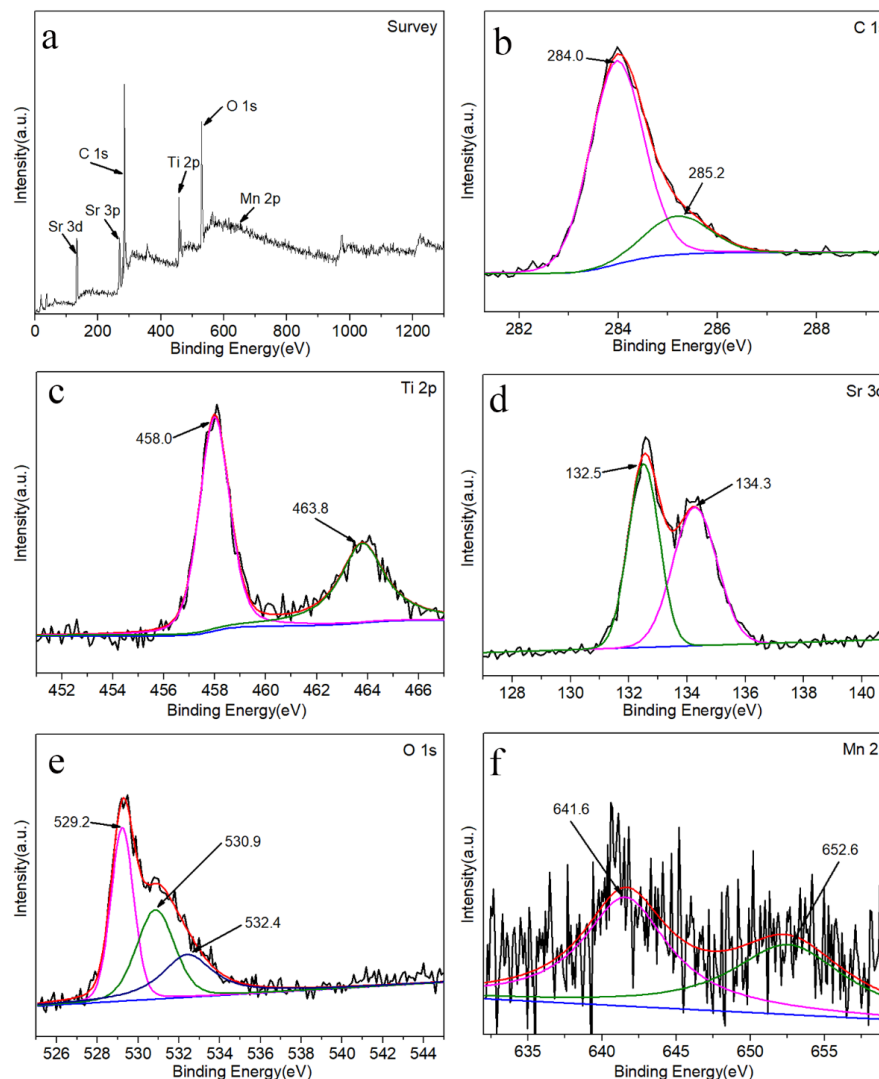

Figure 5. XPS diagram of Mn-SrTiO$_3$@CF sample, (**a**) full spectrum, (**b**) C 1S spectrum, (**c**) Ti 2P spectrum, (**d**) Sr 3D spectrum, (**e**) O 1S spectrum, and (**f**) Mn 2P spectrum.

The EPR test was conducted to further confirm the existence of oxygen vacancies in the Mn-SrTiO$_3$@CF sample, as shown in Figure 6. It can be observed from Figure 6 that the Mn-SrTiO$_3$@CF sample has a strong peak at g ≈ 2.003, indicating the existence of oxygen vacancies in the Mn-SrTiO$_3$@CF sample [34,35]. The generation of oxygen vacancies in the Mn-SrTiO$_3$@CF sample may be caused by the fact that, in the carbonization process of bamboo pulp fibers loaded with SrTiO$_3$, a part of C reacts with O in SrTiO$_3$, and after SrTiO$_3$ is treated at high temperature in argon atmosphere, a part of O in the lattices sheds off, thus forming oxygen defects. The existence of these oxygen vacancies will help to expand the light absorption range of the photocatalyst as well as to improve the charge transfer ability of the Mn-SrTiO$_3$@CF material. Combined with the above analysis of results, it indicated that Mn-SrTiO$_3$@CF composite material rich in oxygen vacancies is successfully prepared, and the doping of Mn will further improve the photocatalytic activity of the material.
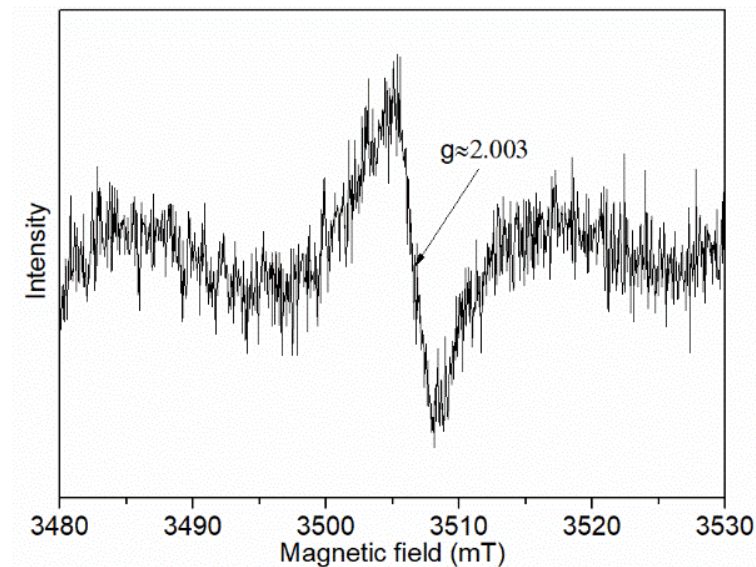
Figure 6. EPR test of the Mn-SrTiO$_3$@CF sample.

　　The photocatalytic hydrogen production performance of composite materials such as SrTiO$_3$@CF and Mn-SrTiO$_3$@CF was tested under simulated sunlight. The test results are shown in Figure 7. Na$_2$S and Na$_2$SO$_3$ were used as sacrificial agents in this experiment. It can be seen from Figure 7 that carbon fibers have no hydrogen production performance under the action of light, while the hydrogen production performance of SrTiO$_3$@CF photocatalytic composite fibers is about 46.90 μmol/g·h. It is presumed that the existence of oxygen vacancies in the SrTiO$_3$@CF material promotes the extension of its light absorption boundary to visible light and enhances the charge transfer ability, which is conducive to improving the photocatalytic property of the material. Meanwhile, the carbon fibers have functions similar to co-catalysts, promoting the migration of photoelectrons [24]. As shown in Figure 7, the hydrogen production capacity of Mn-SrTiO$_3$@CF composite photocatalytic fibers reaches 285.37 μmol/g·h, which is about six times that of the SrTiO$_3$@CF material, which is obviously attributed to the doping of a small amount of Mn ions; the result is similar to the research in [36]. The doping of Mn ions not only promoted the red shift of the light absorption boundary and the extension to visible light, but also improved the separation and migration efficiency of photocarriers. The above test results showed that the existence of oxygen vacancies, the function of carbon fibers similar to a co-catalyst, and the doping of Mn ions significantly improved the hydrogen production performance of Mn-SrTiO$_3$@CF photocatalytic composite fibers.
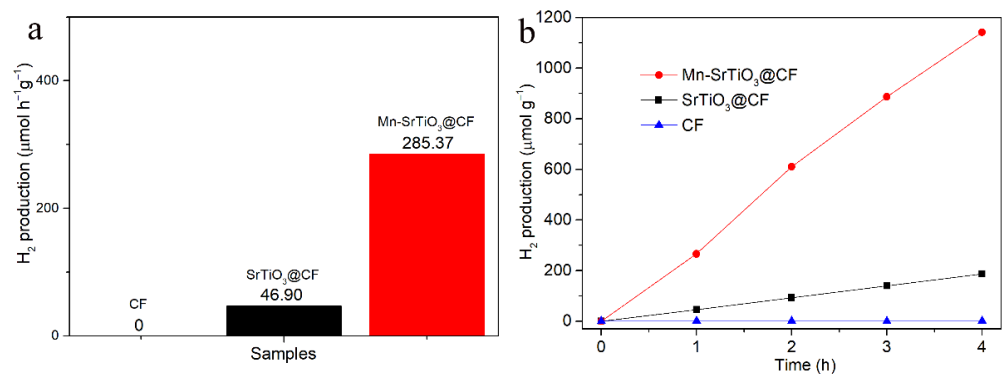

Figure 7. Photocatalytic hydrogen production rate (**a**) and time-dependent hydrogen production amount of different samples (**b**).

The cyclic stability of the Mn-SrTiO$_3$@CF composite catalyst was tested, and the results are shown in Figure 8. After four consecutive tests of cyclic photocatalytic water splitting hydrogen production performance, the average photocatalytic hydrogen production performance of the Mn-SrTiO$_3$@CF composite catalyst is about 267.69 μmol/g·h. There was only a slight decrease over a period of cyclic experiments, indicating that the the Mn-SrTiO3@CF composite catalyst can maintain relatively stable photocatalytic performance in the water splitting hydrogen production reaction.
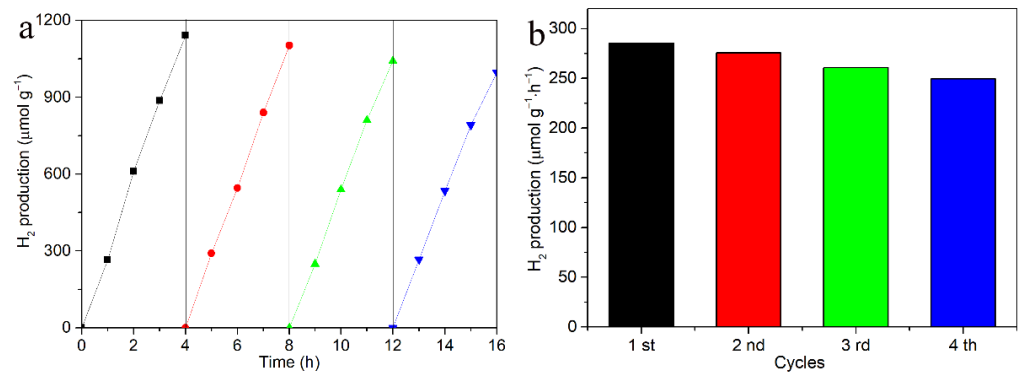

Figure 8. Photocatalytic stability diagram of Mn-SrTiO$_3$@CF composite material. (**a**) Cycle curve of hydrogen production amount, (**b**) The corrresponding histogram.

The light absorption of catalyst materials such as Mn-SrTiO$_3$@CF can be measured by UV–Vis diffuse reflection spectrum test. As shown in Figure 9a, pure SrTiO$_3$ nanoparticles have an obvious characteristic absorption edge at 375 nm, while the light absorption property of SrTiO$_3$@CF is significantly enhanced compared with pure SrTiO$_3$, which mainly comes from the strong light absorption property of carbon fibers. Mn-SrTiO$_3$@CF photocatalytic composite fibers have stronger light absorption property compared with SrTiO$_3$@CF materials, because the doping of Mn reduces the band gap of the composite material and promotes the red shift of the light absorption boundary and the extension to visible light [37]. Mn-SrTiO$_3$@CF and SrTiO$_3$@CF materials have a significant change in the radian of the bottom of the light absorption edge, which is presumed to be because of the existence of oxygen vacancies in the material, reducing the band gap of the catalyst and further enhancing the light absorption property.
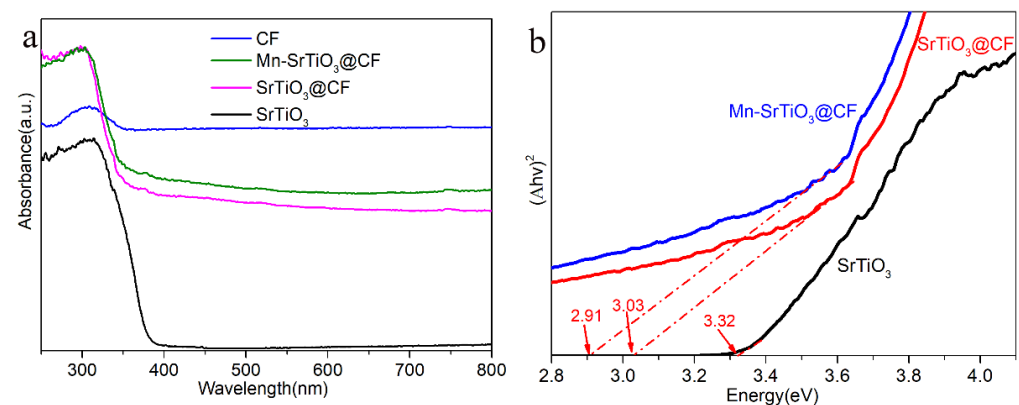

Figure 9. UV–Vis diffuse reflection spectra of samples (**a**) and band gap of the SrTiO$_3$ sample (**b**).

Based on the Kubelka–Munk theory, the band gap (E_g) of semiconductor materials can be calculated according to Equation (1) [38]. As shown in Figure 9b, $h\nu$ is drawn with $(Ah\nu)^2$, from which it can be obtained that the band gap of single SrTiO$_3$ is about 3.32 eV.

Similarly, it can also be calculated that the band gaps of Mn-SrTiO₃@CF and SrTiO₃@CF composites are about 2.91 eV and 3.08 eV, respectively.

$$(Ah\upsilon)^2 = C(h\upsilon - E_g) \tag{1}$$

where A is absorbance in UV–visible diffuse reflection; $h\upsilon$ is photon energy, which is replaced here by the 1024/ wavelength; and C is a constant.

The band structure is an important factor affecting the photocatalytic property, and the flat band potential of the semiconductor catalyst can be calculated using the Mott–Schottky equation (Equation (2)) [38,39].

$$\frac{1}{C^2} = \frac{2}{\varepsilon\varepsilon_0 e N_D}(V - V_{FB} - \frac{k_B T}{e}) \tag{2}$$

where C is the interface capacitance and V_{FB} is the flat band potential.

As shown in Figure 10, the tangent slope of the Mott–Schottky spectral line of SrTiO₃ is positive, indicating that SrTiO₃ is an n-type semiconductor material and the flat band potential of SrTiO₃ is −0.69 eV (calomel electrode, vs. SCE). Based on the fact that the potential of a calomel electrode relative to a standard hydrogen electrode at 25 °C is about 0.24 eV, it can be calculated that the Fermi level corresponding to SrTiO₃ is about −0.45 eV. It is generally believed that the conduction band position of n-type semiconductor is 0.1 eV different from the Fermi level [40], so the conduction band position of SrTiO₃ is −0.55 eV. It can be known from Figure 9b that the band gap of SrTiO₃ is 3.32 eV. It can be calculated that the valence band position of SrTiO₃ is 2.77 eV.
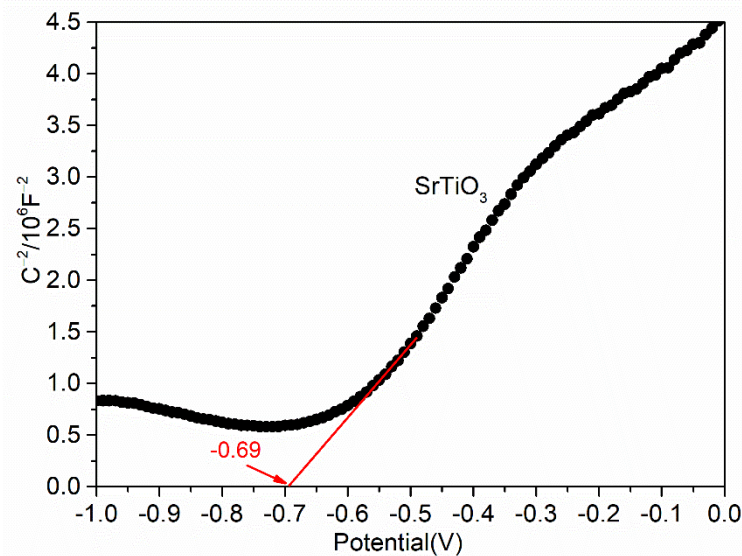

Figure 10. Mott–Schottky plot of the SrTiO₃ sample.

Based on the above research results, we proposed the photocatalytic water splitting hydrogen production mechanism of the Mn-SrTiO₃@CF photocatalytic composite material, as shown in Figure 11.

According to the test results of the UV–Vis diffuse reflection spectrum (Figure 9), it can be calculated that the composite band gaps of the pure SrTiO₃, Mn-SrTiO₃@CF, and SrTiO₃@CF composite materials are about 3.32 eV, 2.91 eV, and 3.08 eV, respectively. The results indicated that the doping of Mn and the existence of oxygen vacancies reduced the band gap of the corresponding material; expanded the light absorption range, which extended to the visible light; and improved the photocatalytic activity. The Mn-SrTiO₃@CF composite material has a large number of oxygen vacancies, which will create a new donor level below the conduction band, constituting an oxygen vacancy state (VOs) and becoming

the capture center of photoelectrons. As shown in Figure 11, under the action of light, the Mn-SrTiO$_3$ composite material produces electrons and holes, and photoelectrons migrate to the conduction band and the oxygen vacancy state (VOs) [41]. Some of the electrons located on the conduction band will migrate to the surface of carbon fibers, and some will migrate to the oxygen vacancy state (VOs), which promotes the separation and migration of photoelectrons and holes, thus improving the photocatalytic property. The electrons on the conduction band and the oxygen vacancy state (VOs) will combine with H$^+$ ions in water to produce hydrogen, while the holes on the valence band will combine with sacrificial agents (Na$_2$S and Na$_2$SO$_3$) in aqueous solution to promote the separation and generation of photoelectron–hole pairs.
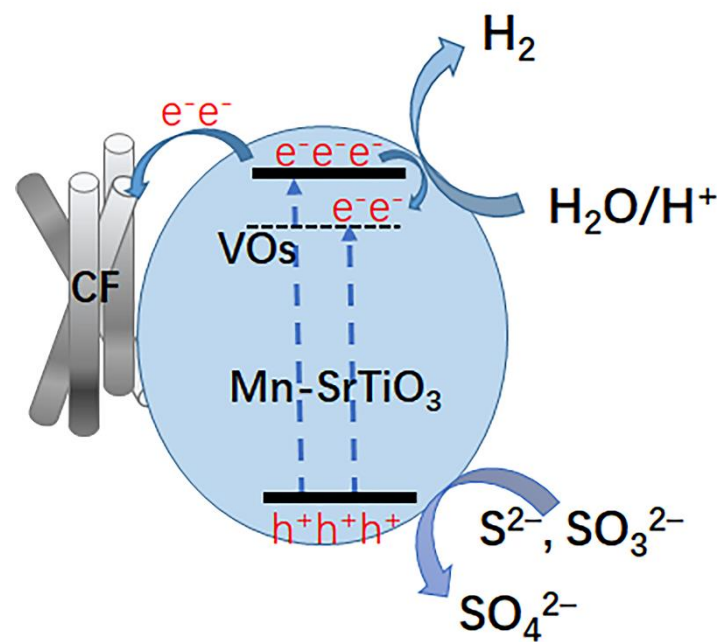

Figure 11. Hydrogen production mechanism of Mn-SrTiO$_3$@CF photocatalytic composite material.

4. Conclusions

In this work, Tencel fibers were taken as the substrate, and SrTiO$_3$@CF and Mn-SrTiO$_3$@CF with a firm structure were successfully obtained through the process route of first loading the semiconductor material on the carrier and then carbonizing the tencel fibers. This solved the problem that the semiconductor materials were difficult to directly load on the surfaces of carbon fibers or easy to shed off because of the smooth surface and few active groups of carbon fibers. The Mn-SrTiO$_3$@CF composite photocatalytic fibers exhibited a higher activity for hydrogen evolution compared with the SrTiO$_3$@CF material. Particularly, the photocatalytic hydrogen production of the Mn-SrTiO$_3$@CF composite catalyst is about 267.69 μmol/g·h with 5% Mn-doped, which is six times that of the SrTiO$_3$@CF material. After modifying SrTiO$_3$@CF with Mn, the light absorption boundary could be extended to the visible light direction, and the separation and migration efficiency of photocarriers could be improved. In addition, SrTiO$_3$@CF and Mn-SrTiO$_3$@CF photocatalytic materials rich in oxygen vacancies were successfully prepared through the high temperature carbonization process. The existence of oxygen vacancies would generate a new donor level below the conduction band, constituting an oxygen vacancy state (VOs) and becoming the capture center of photoelectrons, thus significantly improving the photocatalytic activity. The synergistic effect from Mn doping, oxygen vacancies, the sacrificial agent, and carbon fibers can efficiently absorb photons, transfer photoinduced electrons, restrain carrier recombination, and improve the efficiency of the catalyst hydrogen production.

References

1. Phoon, B.L.; Lai, C.W.; Juan, J.C.; Show, P.L.; Chen, W.H. A review of synthesis and morphology of SrTiO$_3$ for energy and other applications. *Int. J. Energy Res.* **2019**, *43*, 5151–5174. [CrossRef]

2. Liang, Y. Recent advanced development of metal-loaded mesoporous organosilicas as catalytic nanoreactors. *Nanoscale Adv.* **2021**, *3*, 6827–6868. [CrossRef]

3. Kusiak-Nejman, E.; Czyżewski, A.; Wanag, A.; Dubicki, M.; Sadłowski, M.; Wróbel, R.J.; Morawski, A.W. Photocatalytic oxidation of nitric oxide over AgNPs/TiO$_2$-loaded carbon fiber cloths. *J. Environ. Manag.* **2020**, *262*, 110343. [CrossRef] [PubMed]

4. Wang, Y.; Li, J.; Ding, C.; Sun, Y.; Lin, Y.; Sun, W.; Luo, C. Synthesis of surface plasma photocatalyst Ag loaded TiO$_2$ nanowire arrays/graphene oxide coated carbon fiber composites and enhancement of the photocatalytic activity for tetracycline hydrochloride degradation. *J. Photochem. Photobiol. A Chem.* **2017**, *342*, 94–101. [CrossRef]

5. Ma, X.; Zhou, W.; Chen, Y. Structure and photocatalytic properties of Mn-doped TiO$_2$ loaded on wood-based activated carbon fiber composites. *Materials* **2017**, *10*, 631. [CrossRef] [PubMed]

6. Opoku, F.; Govender, K.K.; van Sittert, C.G.C.E.; Govender, P.P. Enhancing Charge Separation and Photocatalytic Activity of Cubic SrTiO$_3$ with Perovskite-Type Materials MTaO$_3$ (M = Na, K) for Environmental Remediation: A First-Principles Study. *ChemistrySelect* **2017**, *2*, 6304–6316. [CrossRef]

7. Hu, Y.; Shen, Z.; Li, B.; Li, S.; Yue, J.; Zhao, G.; Muhler, M.; Wang, X. Solvent effects on photocatalytic anaerobic oxidation of benzyl alcohol over Pt-loaded defective SrTiO$_3$ nanoparticles. *ACS Appl. Nano Mater.* **2021**, *4*, 9254–9264. [CrossRef]

8. Wu, Y.; He, T. Ag loading induced visible light photocatalytic activity for pervoskite SrTiO$_3$ nanofibers. *Spectrochim. Acta Part A Mol. Biomol. Spectrosc.* **2018**, *199*, 283–289. [CrossRef]

9. Grabowska, E.; Marchelek, M.; Klimczuk, T.; Lisowski, W.; Zaleska-Medynska, A. TiO$_2$/SrTiO$_3$ and SrTiO$_3$ microspheres decorated with Rh, Ru or Pt nanoparticles: Highly UV–vis responsible photoactivity and mechanism. *J. Catal.* **2017**, *350*, 159–173. [CrossRef]

10. Li, X.; Ge, Z.; Xue, F.; Liu, H.; Lyu, B.; Liu, M. Lattice-oriented contact in Pd/SrTiO$_3$ heterojunction for rapid electron transfer during photocatalytic H$_2$ production. *Mater. Res. Bull.* **2020**, *123*, 110722. [CrossRef]

11. Tolod, K.; Bajamundi, C.; de Leon, R.; Sreearunothai, P.; Khunphonoi, R.; Grisdanurak, N. Visible light-driven photocatalytic hydrogen production using Cu-doped SrTiO$_3$. *Energy Sour. Part A Recovery Util. Environ. Eff.* **2016**, *38*, 286–294. [CrossRef]

12. Chiang, T.H.; Lyu, H.; Hisatomi, T.; Goto, Y.; Takata, T.; Katayama, M.; Minegishi, T.; Domen, K. Efficient photocatalytic water splitting using Al-doped SrTiO$_3$ coloaded with molybdenum oxide and rhodium–chromium oxide. *ACS Catal.* **2018**, *8*, 2782–2788. [CrossRef]

13. Wu, G.; Li, P.; Xu, D.; Luo, B.; Hong, Y.; Shi, W.; Liu, C. Hydrothermal synthesis and visible-light-driven photocatalytic degradation for tetracycline of Mn-doped SrTiO$_3$ nanocubes. *Appl. Surf. Sci.* **2015**, *333*, 39–47. [CrossRef]

14. Thanh, T.D.; Phan, T.; Van Minh, N.; Lee, J.S.; Yu, S. Influence of Mn Doping on the Crystal Structure, and Optical and Magnetic Properties of SrTiO$_3$ Compounds. *IEEE Trans. Magn.* **2014**, *50*, 1–4.

15. Bentour, H.; El Yadari, M.; El Kenz, A.; Benyoussef, A. DFT study of electronic and optical properties of (S–Mn) co-doped SrTiO$_3$ for enhanced photocatalytic hydrogen production. *Solid State Commun.* **2020**, *312*, 113893. [CrossRef]

16. Yang, C.; Liu, T.; Cheng, Z.; Gan, H.; Chen, J. Study on Mn-doped SrTiO$_3$ with first principle calculation. *Phys. B Condens. Matter* **2012**, *407*, 844–848. [CrossRef]

17. Tan, H.; Zhao, Z.; Zhu, W.-b.; Coker, E.N.; Li, B.; Zheng, M.; Yu, W.; Fan, H.; Sun, Z. Oxygen vacancy enhanced photocatalytic activity of pervoskite SrTiO$_3$. *ACS Appl. Mater. Interfaces* **2014**, *6*, 19184–19190. [CrossRef]

18. Ye, K.; Li, K.; Lu, Y.; Guo, Z.; Ni, N.; Liu, H.; Huang, Y.; Ji, H.; Wang, P. An overview of advanced methods for the characterization of oxygen vacancies in materials. *TrAC Trends Anal. Chem.* **2019**, *116*, 102–108. [CrossRef]

19. Sarkar, A.; Khan, G.G. The formation and detection techniques of oxygen vacancies in titanium oxide-based nanostructures. *Nanoscale* **2019**, *11*, 3414–3444. [CrossRef]

20. Li, H.; Li, J.; Ai, Z.; Jia, F.; Zhang, L. Oxygen vacancy-mediated photocatalysis of BiOCl: Reactivity, selectivity, and perspectives. *Angew. Chem. Int. Ed.* **2018**, *57*, 122–138. [CrossRef]

21. Pan, X.; Yang, M.-Q.; Fu, X.; Zhang, N.; Xu, Y.-J. Defective TiO$_2$ with oxygen vacancies: Synthesis, properties and photocatalytic applications. *Nanoscale* **2013**, *5*, 3601–3614. [CrossRef] [PubMed]
22. Lei, S.; Qin, C.; Tang, X.; Zhong, J.; Li, J.; Chen, J. Spiral carbon fibers modified Bi$_2$WO$_6$ with enhanced photocatalytic activity. *J. Phys. Chem. Solids* **2020**, *141*, 109430. [CrossRef]
23. Zhang, C.; Han, P.; Lu, X.; Mao, Q.; Qu, J.; Li, Y. Preparation and photocatalytic activity characterization of activated carbon fiber–BiVO4 composites. *RSC Adv.* **2018**, *8*, 24665–24672. [CrossRef] [PubMed]
24. Tang, G.; Abas, A.; Wang, S. Photocatalytic Degradation and Hydrogen Production of TiO$_2$/Carbon Fiber Composite Using Bast as a Carbon Fiber Source. *Int. J. Photoenergy* **2018**, *2018*, 4954039. [CrossRef]
25. Lu, D.; Ouyang, S.; Xu, H.; Li, D.; Zhang, X.; Li, Y.; Ye, J. Designing Au surface-modified nanoporous-single-crystalline SrTiO$_3$ to optimize diffusion of surface plasmon resonance-induce photoelectron toward enhanced visible-light photoactivity. *ACS Appl. Mater. Interfaces* **2016**, *8*, 9506–9513. [CrossRef]
26. Ramos, M.; Bonelli, P.; Cukierman, A.; Carrott, M.R.; Carrott, P. Influence of thermal treatment conditions on porosity development and mechanical properties of activated carbon cloths from a novel nanofibre-made fabric. *Mater. Chem. Phys.* **2009**, *116*, 310–314. [CrossRef]
27. Zhang, X.; Li, Z.; Zeng, B.; Li, C.; Han, H. EPR study of charge separation associated states and reversibility of surface bound superoxide radicals in SrTiO$_3$ photocatalyst. *J. Energy Chem.* **2022**, *70*, 388–393. [CrossRef]
28. Xia, Y.; He, Z.; Su, J.; Liu, Y.; Tang, B. Fabrication and photocatalytic property of novel SrTiO$_3$/Bi$_5$O$_7$I nanocomposites. *Nanoscale Res. Lett.* **2018**, *13*, 1–9. [CrossRef]
29. Dong, Y.; Zhu, X.; Pan, F.; Deng, B.; Liu, Z.; Zhang, X.; Huang, C.; Xiang, Z.; Lu, W. Mace-like carbon fiber/ZnO nanorod composite derived from typha orientalis for lightweight and high-efficient electromagnetic wave absorber. *Adv. Compos. Hybrid Mater.* **2021**, *4*, 1002–1014. [CrossRef]
30. Jiang, D.; Sun, X.; Wu, X.; Shi, L.; Du, F. Hydrothermal synthesis of single-crystal Cr-doped SrTiO$_3$ for efficient visible-light responsive photocatalytic hydrogen evolution. *Mater. Res. Express* **2020**, *7*, 015047. [CrossRef]
31. Shi, J.; Chen, J.; Li, G.; An, T.; Yamashita, H. Fabrication of Au/TiO$_2$ nanowires@ carbon fiber paper ternary composite for visible-light photocatalytic degradation of gaseous styrene. *Catal. Today* **2017**, *281*, 621–629. [CrossRef]
32. Wong, C.P.P.; Lai, C.W.; Lee, K.M.; Pan, G.T.; Huang, C.M.; Juan, J.C.; Yang, T.C.K. Enhancement of discharge capacity and energy density by oxygen vacancies in nickel doped SrTiO$_3$ as cathode for rechargeable alkaline zinc battery. *Electrochim. Acta* **2022**, *404*, 139705. [CrossRef]
33. Huang, Y.; Yu, Y.; Yu, Y.; Zhang, B. Oxygen vacancy engineering in photocatalysis. *Sol. RRL* **2020**, *4*, 2000037. [CrossRef]
34. Hao, L.; Huang, H.; Zhang, Y.; Ma, T. Oxygen vacant semiconductor photocatalysts. *Adv. Funct. Mater.* **2021**, *31*, 2100919. [CrossRef]
35. Li, C.-Q.; Yi, S.-S.; Liu, Y.; Niu, Z.-L.; Yue, X.-Z.; Liu, Z.-Y. In-situ constructing S-scheme/Schottky junction and oxygen vacancy on SrTiO$_3$ to steer charge transfer for boosted photocatalytic H$_2$ evolution. *Chem. Eng. J.* **2021**, *417*, 129231. [CrossRef]
36. Yang, H.; Sun, Y.; Pei, W.; Wang, X.; Luo, Y.; Jin, Y.; Zhang, Y.; Yi, X.; Li, Q.; Fan, F. Insight into energy level modulation via Mn doping solid solutions for enhanced photocatalytic hydrogen production. *Inorg. Chem. Commun.* **2022**, *135*, 109041. [CrossRef]
37. Suárez-Vázquez, S.I.; Cruz-López, A.; Molina-Guerrero, C.E.; Sánchez-Vázquez, A.I.; Macías-Sotelo, C. Effect of dopant loading on the structural and catalytic properties of Mn-doped SrTiO$_3$ catalysts for catalytic soot combustion. *Catalysts* **2018**, *8*, 71. [CrossRef]
38. Li, X.; He, C.; Zuo, S.; Yan, X.; Dai, D.; Zhang, Y.; Yao, C. Photocatalytic nitrogen fixation over fluoride/attapulgite nanocomposite: Effect of upconversion and fluorine vacancy. *Sol. Energy* **2019**, *191*, 251–262. [CrossRef]
39. Xu, H.; Wang, Y.; Dong, X.; Zheng, N.; Ma, H.; Zhang, X. Fabrication of In$_2$O$_3$/In$_2$S$_3$ microsphere heterostructures for efficient and stable photocatalytic nitrogen fixation. *Appl. Catal. B Environ.* **2019**, *257*, 117932. [CrossRef]
40. Wang, Y.; Zeng, Y.; Chen, X.; Wang, Q.; Guo, L.; Zhang, S.; Zhong, Q. One-step hydrothermal synthesis of a novel 3D BiFeWOx/Bi$_2$WO$_6$ composite with superior visible-light photocatalytic activity. *Green Chem.* **2018**, *20*, 3014–3023. [CrossRef]
41. Wang, H.; Yong, D.; Chen, S.; Jiang, S.; Zhang, X.; Shao, W.; Zhang, Q.; Yan, W.; Pan, B.; Xie, Y. Oxygen-vacancy-mediated exciton dissociation in BiOBr for boosting charge-carrier-involved molecular oxygen activation. *J. Am. Chem. Soc.* **2018**, *140*, 1760–1766. [CrossRef]